Title
Peptide-Programmable Nanoparticle Superstructures with Tailored Electrocatalytic Activity

Journal
ACS Nano, 12(7)

ISSN
1936-0851

Authors
Kang, Eun Sung
Kim, Yong-Tae
Ko, Young-Seon
et al.

Publication Date
2018-07-24

DOI
10.1021/acsnano.8b01146

Peer reviewed

HHS Public Access

Author manuscript

ACS Nano. Author manuscript; available in PMC 2019 June 08.

Published in final edited form as:

ACS Nano. 2018 July 24; 12(7): 6554–6562. doi:10.1021/acsnano.8b01146.

Peptide-Programmable Nanoparticle Superstructures with Tailored Electrocatalytic Activity

Eun Sung Kang[†,▲], **Yong-Tae Kimu**[†,▲], **Young-Seon Ko**[†,▲], **Nam Hyeong Kim**[†], **Geonhee Cho**[▽], **Yang Hoon Huh**[§], **Ji-Hun Kim**[†], **Jiyoung Nam**[†], **Trung Thanh Thach**[†], **David Youn**[⊥], **Young Dok Kim**[‡], **Wan Soo Yun**[‡], **William F. DeGrado**[‖], **Sung Yeol Kim**[○], **Paula T. Hammond**[◆], **Jaeyoung Lee**[#], **Young-Uk Kwon**[‡], **Don-Hyung Ha**[*,▽], and **Yong Ho Kim**[*,†,‡,□,●]

[†]SKKU Advanced Institute of Nanotechnology (SAINT), Sungkyunkwan University, Suwon 16419, Republic of Korea

[‡]Department of Chemistry, Sungkyunkwan University, Suwon 16419, Republic of Korea

[§]Electron Microscopy Research Center, Korea Basic Science Institute, Cheongju 28119, Republic of Korea

[‖]Department of Pharmaceutical Chemistry, University of California San Francisco, San Francisco, California 94158, United States

[⊥]Department of Chemistry, The Pennsylvania State University, University Park, Pennsylvania 16802, United States

[#]School of Environmental Science and Engineering, Ertl Center for Electrochemistry and Catalysis, Research Institute for Solar and Sustainable Energies (RISE), Gwangju Institute of Science and Technology (GIST), Gwangju 61005, Republic of Korea

[▽]School of Integrative Engineering, Chung-Ang University, Seoul 06974, Republic of Korea

[○]School of Mechanical Engineering, Kyungpook National University, Daegu 702-701, Republic of Korea

[◆]Department of Materials Science and Engineering, Massachusetts Institute of Technology, Cambridge, Massachusetts 02139, United States

[●]Center for Neuroscience Imaging Research, Institute for Basic Science (IBS), Suwon 16419, Republic of Korea

[*]**Corresponding Authors** dhha@cau.ac.kr (D.-H.H.). yhkim94@skku.edu (Y.H.K.).

[□]**Present Address:** Sungkyunkwan University, SKKU Advanced Institute of Nanotechnology (SAINT), Jangan-gu, cheoncheon-dong, 300, Suwon 400-746, Korea.

[▲]E.S.K., Y.-T.K., and Y.-S.K. contributed equally

ASSOCIATED CONTENT

Supporting Information

The Supporting Information is available free of charge on the ACS Publications website at DOI: 10.1021/acsnano.8b01146.

Additional experimental details about synthesis and characterization of peptide-mediated nanoparticle super-structures, explanation of detail design process for specifying specific nucleation sites in superstructures, 3-D reconstruction data by various angles, and negative control data. (PDF)

Three-dimensional reconstruction movie (MPG)

The authors declare no competing financial interest.

Abstract

Biomaterials derived *via* programmable supramolecular protein assembly provide a viable means of constructing precisely defined structures. Here, we present programmed superstructures of AuPt nanoparticles (NPs) on carbon nanotubes (CNTs) that exhibit distinct electrocatalytic activities with respect to the nanoparticle positions *via* rationally modulated peptide-mediated assembly. *De novo* designed peptides assemble into six-helix bundles along the CNT axis to form a suprahelical structure. Surface cysteine residues of the peptides create AuPt-specific nucleation site, which allow for precise positioning of NPs onto helical geometries, as confirmed by 3-D reconstruction using electron tomography. The electrocatalytic model system, i.e., AuPt for oxygen reduction, yields electrochemical response signals that reflect the controlled arrangement of NPs in the intended assemblies. Our design approach can be expanded to versatile fields to build sophisticated functional assemblies.

Graphical Abstract

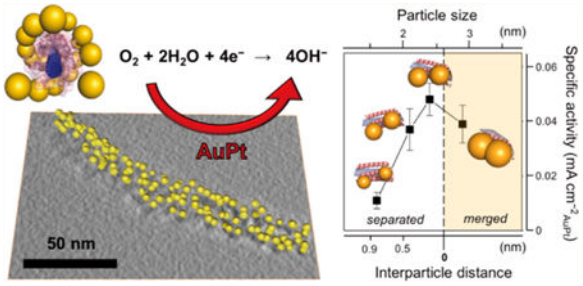

Keywords

supramolecular protein self-assembly; artificialy designed peptide; nanoparticle superstructure; electron tomography; peptide-based superstructure 3-D reconstruction; peptide-based catalyst; electrocatalytic oxygen reduction

Supramolecular protein assemblies afford a wide range of hierarchically organized architectures that mimic natural systems.[1–3] Artificially designed peptides are particularly interesting because they are programmed to assemble into desired superstructures that exhibit structural diversity on the nanometer and micrometer scales. Moreover, the peptide sequence can be encoded to provide tailored surfaces, enabling the arrangement of inorganic nanoparticles (NPs) into functional geometries.[4–10]

NP superstructures have notable physicochemical properties that are applicable in catalysis, plasmonics, molecular recognition, and energy conversion systems.[11–16] To tailor such properties, considerable effort has been devoted to modifying the size, shape, composition, and arrangement of NPs.[17–24] In particular, NPs with controlled spatial arrangements have been shown to evolve remarkable collective properties, e.g., strong optical chirality at visible wavelengths upon chiral assemblies of metal NPs[14] and high p-type conductivity in discrete assemblies of binary semiconductor NPs.[24] These controlled arrangements of NPs can be achieved by exploiting biomolecular templates; this feature is due to their ability to selectively recognize, bind, and hold NPs in precise locations.[25–28] Moreover, increased

control of superstructures with enhanced functionality can enable the manipulation of evolved collective properties for the development of functional nanomaterials.[29–34]

In this paper, we adopt a rational protein-design approach to engineer geometrically predefined, peptide-based arrangements of NP superstructures that are anchored on single-walled carbon nanotubes (SWNTs). For this purpose, we designed the peptide by structurally encoding the information for bifunctional specific recognition, which includes (1) the nanotube-specific face that interacts with the SWNT, wrapping around it in a suprahelical pattern, and (2) the metal-specific face that binds the NPs, arranging them at predefined positions. By showing that the conducting SWNT and metal NPs can be combined, we demonstrate the potential applicability of a system for an electrochemical reaction. The NPs are well-organized on the peptide/SWNT template at precise positions that are commensurate with the metal-specific nucleation sites, as predicted from the programmed peptide sequence; this is confirmed by changes in the electrochemical signals.

RESULTS AND DISCUSSION

We synthesized NP superstructures, as illustrated in Figure 1a. The 30-residue peptide designed in a previous *de novo* study, i.e., HexCoil-Ala, was used as a structural template to coat the surfaces of chiral SWNTs (HC/SWNT).[35] Subsequent peptide design optimized the geometry and energy parameters to achieve the desired interfacial interactions for the assemblies. The resulting HexCoil-Ala variants assemble into an antiparallel hexameric bundle that forms a superhelix along the SWNT axis. The hexameric bundle is formed *via* two different helix–helix interactions, each resembling an Ala-coil or Leu zipper (Figure S1). While the Ala-rich inner surfaces interact with the aromatic surface of the SWNT, the outer surfaces (exposed to the solvent) can bind NPs if the surface residue propensities are appropriately engineered (Figures 1b,c). The position of NPs is dependent on the engineered propensity profiles in the peptide sequences, facilitating the manipulation of superstructure geometries.

We systematically revised the amino acid compositions of HexCoil-Ala to define the geometry of NP superstructures with reasonable accuracy. Cys residues replaced several of the existing residues to bind metal NPs because the Cys sulfhydryl groups have a strong chemical affinity for metals.[26,35] If the interpeptide packing stability is not taken into account when introducing Cys for NP nucleating, the number of possible sequence combinations exceeds one billion (1073 741793). However, we avoided abrupt sequence changes that can disturb the superhelical bundle. Therefore, we selected only two residue positions in the aligned sequence for Cys-substitution. This restricts the possible number of sequences to 2-combinatorial selection from 30 positions ($_{30}C_2$), which results in 435 possible sequences. Further selection rules considered the inclusion of fully solvent-exposed residue sites, whereas interhelical-facing and SWNT-contacting sites were excluded. Also, both terminal positions of the peptide were ruled out in order to conserve the end-to-end contact of hexameric bundles arranged along the SWNT axis. These rational selection rules further reduce the number of possible positions for Cys-substitutions to six, restricting the number of design templates to $_6C_2$, or 15 sequences, each of which provides a special NP superstructure (Figures S2, S3, and S4 and Table S1). On the basis of the geometry of the

Cys positions computed from the well-established helical-bundle parametric model, we determined the parameters for precisely defining the predicted NP superstructures (see the Supporting Information for details). In this model, each NP site is composed of two Cys residues in close proximity within the antiparallel dimeric unit (inset of Figure 1c); the tiny NPs nucleated at each of the two Cys sites will eventually merge into one large NP.[8,35]

The mathematical modeling results indicate that the 15 superstructures can be classified into two categories, i.e., 3 × 2-fold and three-fold helical arrays, which differ in their configurations of NPs in the antiparallel dimeric unit (Figure 2a and Figure S2). The 3 × 2-fold array has 3-fold helices with a 2-fold screw rotation axis. In the antiparallel dimer, two distinct types of distances can be defined between adjacent Cys residues: one is on a monomer (d_{intra}), whereas the other is formed at the dimeric interface (d_{inter}). For the 3 × 2-fold helices, each monomer has one NP because the growing nuclei within the monomer are merged before intermonomeric NPs can merge, as $d_{intra} < d_{inter}$. Contrastingly, the three-fold helices result from each dimer sharing the NPs at its interface, as $d_{intra} > d_{inter}$.

These geometrically specified models are characterized by their distinctive structural features, including the superhelical pitch and interparticle distance (ID), which can predict the particle size that maximizes the chemical reactivity (e.g., the catalytic activity) in a given template.

To test this attribute, we measured the electrochemical response of the precisely arranged AuPt NPs and correlated it with the NP arrangement geometry. The HexCoil-Ala with its *m*th and *n*th residues changed to Cys, (*m*,*n*)-CysHC, was used to define the NP arrays, designated as (*m*,*n*). For the ID calculation, the computational models depicted in Figure 2a were used. The geometry of three first-nearest neighboring NPs adjacent to a central NP dictates the interfacial ID. The distances between NPs can be classified into three types like Ala coil-like (interparticle distance (ID) type i), Leu zipper-like (ID type ii), and end-to-end helical interfaces (ID type iii); these values were computed as in Figure 2b. The calculated three types of interparticle distances were different for individual submodels within the 3 × 2-fold helical array, whereas in the three-fold array, ID type ii was invariant in all submodels. The other two types of interparticle distances, the intrahelical ID type i (spacing at the Ala-Ala) and interhelical ID type iii (end-to-end interfaces), aligned along the SWNT axis, were the only variables that determined the interparticle distance, simplifying interpretation of the effect of NP-NP distance on the electrochemical response. So, we chose the three-helix model to test the structure–function correlation efficiently. Furthermore, we could classify the three-fold helical array model into two modes, linear helical array mode and loose linear helical array mode, depending on the number of particles that can be generated per unit volume. As a result, considering the catalytic activity characteristics, we excluded the “loose linear helical array mode” with relatively few NPs per unit volume by their sharing pattern sulfhydryl group and finally selected the four ideal models corresponding to the “linear helical array mode” (Figure S3).

The AuPt NP superstructures were arranged on the peptide templates assembled on the SWNT (Figure 1). The addition of two metal precursors ($AuCl_4^-$ and $PtCl_6^{2-}$) followed by a reductant ($NaBH_4$) to the HC/SWNT suspension led to the formation of AuPt NPs

(AuPt/HC/SWNT). Transmission electron microscopy (TEM) images in Figure 3a reveal NPs with diameters (ø) of ~3 nm assembled around the SWNT. The fibrous AuPt/HC/SWNT assemblies were several micrometers long. X-ray diffraction showed that the individual AuPt NPs were alloyed and had a face-centered cubic structure (Figure S5). X-ray diffraction peaks of the AuPt NPs were located between Au and Pt reference peaks and not separated into Au and Pt peaks, indicating that the AuPt NPs were not phase-segregated. In addition, high-resolution TEM (HRTEM) images revealed that the AuPt NPs did not have core–shell structures (Figure S6). Scanning TEM coupled with energy-dispersive X-ray spectroscopy (STEM-EDS) elemental mapping images confirmed that both Au and Pt were distributed uniformly over the template, implying that the NPs are well-alloyed (Figure 3b).

To fully resolve the three-dimensional structures, the analysis using only TEM can be limited since only two-dimensional orthographic images are utilized for the structural analysis. Therefore, 3-D reconstruction models are ideal and intuitive proof of three-dimensionally arranged systems with NPs controlled by our exquisitely designed peptide structures. We have performed an electron tomography for 3-D reconstructions to clearly confirm our complicated nanostructures. The total 51 tilt images of the (8,26) NPs sample were recorded with a Bio-High Voltage Electron Microscope by tilting from –50° to +50° with 2° increments (Figure S7), and 3-D models were reconstructed through the object surface rendering and 3-D volume modeling (Figure 3c). As the digitized tilt series images were aligned and tomographically reconstructed, it was confirmed that the array of AuPt NPs produced by our peptides is structured into a three-dimensional volume, not a two-dimensional plane (Figure 3c and video in Supporting Information). Furthermore, the helical-bundle parametric model based on the theoretical geometries was compared to a 3-D reconstruction model, elucidating the arrangement of NPs in helical geometries (Figure 3d). There were substantial correlations between the AuPt NPs (yellow dots) of the 3-D reconstruction model and the theoretical helical model (green line) in both the plane and vertical phase (Figure 3d,e). This is a direct indication that our NP arrangement model is well-controlled by the programmable peptides for the precise positions suggested by theoretical calculations, demonstrating that NP arrangements can be effectively controlled through elaborately designed and programmed peptides.

To prove that AuPt NPs in the superstructure were not randomly nucleated on the peptides, a controlled experiment was constructed using the peptide (Non-Cys HexCoil-Ala), which does not contain Cys residues from the designed peptide HexCoil-Ala but still adheres to nanotubes. The TEM images (Figure S8) confirmed that Non-Cys HexCoil-Ala peptides arranged along the surface of CNTs, but no NP was grown along the CNTs and NPs were highly aggregated at the random sites. This controlled experiment indicated that the AuPt NPs are nucleated site-specifically on the Cys residue of our programmatically designed peptide.

According to the calculation, (8,26) NPs should coalesce when their size becomes greater than 2.6 nm (Figure 2c). The interparticle spacing decreases as the observed particle size increases from 1.6 to 2.9 nm (Figure 3f). Although we can confirm that the statistical TEM observation data and the computational data have a similar pattern (Figure 3g), it is insufficient to conclude the precise point of coalescence solely determined by TEM. To

further verify the successful design of the NP geometry, we measured the oxygen reduction reaction (ORR) on the AuPt NPs. The electrochemical response was dependent on the availability of NP surfaces, reflecting the NP superstructure that determines the active surface sites of NPs.

AuPt has higher activity than typical Pt electrocatalysts due to the synergistic properties of the bimetallic system; i.e., Au atoms surrounding Pt can inhibit the formation of Pt–OH bonds on the surface, which requires O_2 dissociation, thereby catalyzing ORR.[36] Since Au has higher electronegativity than Pt, the charges transferred from Pt to Au, increasing the d-band vacancy of PtAu.[36] Normally, the ORR kinetics increase with increased availability of active terrace sites on the growing NPs as their diameter increases from 1 to 10 nm. A particularly large increase in ORR has been reported for particles sized from 1 to 3 nm[37–39]

Contrastingly, we expected that the specific activity (SA) would not be changed upon reaching the NP size where coalescence is predicted to occur (for NPs ranging in size from 1.6 to 2.9 nm). The trend in SA (Figure 4a, specific mass activity in Figure S9) was in good agreement with the predictions of the models (Figure 3f). The SA increased when the NPs grew from 1.6 to 2.4 nm in ø, but the size-dependence vanished beyond 2.9 nm. This decrease in SA is due to the coalesced NPs. When the NPs with randomly oriented crystallographic facets merged (Figure S6), the boundary interface contained numerous defects containing undercoordinated sites.[40] These sites reduce the ORR due to their strong binding affinity to O-containing intermediates.[38,39] Although detailed coordination calculations can better describe the effect of undercoordinated sites on the ORR,[41] the reduced ORR has been well-established empirically;[37–39,41] this is consistent with the decreasing SA that occurred with an increasing number of defect sites beyond the NP coalescence, as calculated here. The specific activity of (8,22), (8,19), and (12,19) also supported the success of our NP array design strategy (Figure 4a). The NP size expected to result in merging in (8,22) and (8,19) was 2.3 and 1.8 nm, respectively. Consistent with the calculation and the results obtained from (8,26), the specific activities decreased upon reaching these respective calculated sizes. For (8,19), when the NPs grew beyond the point of merging, the specific activity increased again, presumably due to the active sites that continued to amass. The size-dependent specific activity behavior was also confirmed in the assembly (12,19), which exhibited increasing activity beyond the point of particle aggregation ($ø_c$ =1.3 nm).

The losses of specific activity at the NP aggregation transition region also support the success of our design strategy (Figure 4b). The losses, calculated using the relationship $[(j_{k,f} - j_{k,m})/j_{k,m}] \times 100$, where $j_{k,f}$ is the first data point after the maximum activity, j_{km}, past the aggregation, were 33%, 23%, and 19% for (8,19), (8,22), and (8,26), respectively. These measured losses correlated with the overlapped surface of NPs upon aggregation. The overlapped proportion, estimated using the formula for the surface area of a spherical NPs intersected by a plane, was 8.3%, 6.5%, and 8.3% for (8,19), (8,22), and (8,26), respectively (Figure S10).

The ORR polarizations of AuPt/HC/SWNT with varying NP sizes were measured to obtain the SA values (Figure 4c). The SA was defined as the kinetic current normalized to the

electrochemical surface area of Au and Pt; each of these elements is involved in Au oxide reduction and H^+ desorption from Pt, as determined *via* cyclic voltammetry (Figure S11). The electrocatalytic results show that our NP assemblies were achieved as intended. Further work will determine the attributes embodied in our model. One of the attributes discussed here is the particle size when the particle position is constrained by predefined peptide sequences. NPs with the largest size (before aggregation) would show the highest catalytic activity. The peptide sequences can be further optimized to enhance the catalyst performance. Regarding ORR enhancement, which is a current challenge in fuel cell technologies,[42] the designed peptides can provide a remarkable direction for advanced electrocatalysts.

CONCLUSIONS

In summary, we demonstrate a rational approach that uses a genetically engineered peptide to define the assembly geometry for NP superstructures on SWNTs. Bifunctional surface recognition, which is encoded in the peptide, interlinks the conducting SWNTs and the electrocatalytically active NPs. With the enhanced functionality, we can prepare a peptide-based electrocatalyst with a programmed, specific super-structure. The programmable ability of the peptide regulates the geometric position of the NPs but not their random distribution; this allows us to fine-tune the functional properties of the NP assemblies. To assess the feasibility of the positioning, we used a model system (i.e., AuPt NP assembly) for the ORR. This designed system shows the intended ORR activity trends, which are closely correlated with the results of the theoretical predictions for NP arrangement. The versatility of peptide design in a functional, predictable manner will enable exceptional collective properties to be tailored with well-organized functional structures.

EXPERIMENTAL SECTION

Peptide Assembly.

We used the 30-residue α-helical peptide previously designed *via* standard computational-design techniques to assemble NPs into well-organized superstructures on a single-walled carbon nanotube (SWNT).[35] In searching for the optimal peptide sequences, we considered two factors: (1) peptide packing geometry matching the symmetry of the chiral SWNT surface and (2) interfacial interactions between entities, i.e., helix–helix and helix–SWNT, minimizing the total energy for stabilization. The resulting optimal amino acid sequence is AE AESALEY AQQALEK AQLALQA ARQALKA Alanine residues placed on the *a* heptad position are programmed to interact with the SWNT, so this peptide is called HexCoil-Ala (Figure S1a). The peptide assembles into an antiparallel hexamer around the SWNT (Figure S1b). Two geometrically different alanine coil-like and leucine zipper-like interfaces are defined in the hexamer. The hydrophobic interaction between the apolar residues at the *d* and *e* positions induces interfacial stabilization. Favorable head-to-tail interactions between adjacent hexamers (e.g., hydrogen bonding between N- and C-termini of the two helices) create a superhelical structure along the SWNT axis (Figure S1c).

Model Simulation of Nanoparticle Arrangements.

To bind AuPt NPs on the target surface, the peptide sequences were partially permutated with cysteine amino acids by virtue of their highly selective affinity to metals. Sequence substitution was implemented without destroying the optimal helix–helix and helix–SWNT interactions. We first picked out six outward-facing nucleation sites, E8, Q12, E15, L19, Q22, and Q26, from the 30 amino acid sequences and, then, randomly chose two from the selected six sites to obtain 15 different possible sequences (Figure S2a). The subsequent reduction process of precursors created nuclei on the cysteine sites, and the nuclei grew in size to form NPs. When the particle size exceeds 1.3 nm, the growing particles in close proximity should coalesce due to their fixation by the cysteine residues situated at a distance range 5.3–12.7 A apart (Table S1). Consequently, two adjacent cysteine residues provide one metal-nucleation site, and their midpoint dictates the position of a metal NP. Four possible cysteine–cysteine distances were considered as candidates defining the particle position within two end-to-end antiparallel dimers: one intracysteine distance, $\boldsymbol{d}_{XY}$ (=$\boldsymbol{d}_{X'Y'}$), on a monomer, and three intercysteine distances, $\boldsymbol{d}_{XX'}$, $\boldsymbol{d}_{YY'}$, and $\boldsymbol{d}_{XY'}$ (=$\boldsymbol{d}_{X'Y}$), formed between monomers (Figures S2b and S3). The four distance values were calculated and compared to obtain the smallest one in each permutated peptide model (refer to Table S1), which, eventually, defines the NP arrangement.

Using the above particle-positioning procedure, we simulated the 15 different sequence combinations to define their NP arrangements. Using the simulated models, these arrangements can be classified into two categories, 3 × 2-helical and three-helical arrays, depending on the relationship between intracysteine distances ($d_{intra} = d_{XY}$) and intercysteine distances ($d_{inter} = d_{XX'}$, $d_{YY'}$, or $d_{XY'}$) (Figure 2a and Figure S2c). The 3 × 2-fold array has 3-fold helices with a 2-fold screw rotation axis. For these helices, each monomer has one NP because the growing nuclei within the monomer are merged before intermonomeric NPs can merge, as $d_{intra} < d_{inter}$ Contrastingly, the 3-fold helices result from each dimer sharing the NPs at its interface, as $d_{intra} < d_{inter}$. Of the total 15 models, eight models involve the 3 × 2-helical array and the others the three-helical array.

Theoretical Calculation of Distances between Nanoparticles within Superstructures.

The simulated models provide geometric information about the helical NP structures, such as interparticle distance, helical pitch, and angle. To acquire the interparticle distance information, we used the mathematical formulation with the (x, y, z) coordinates of NPs. The parametric equations of a helix can describe the NP arrangements because the NPs are bound to the underlying peptides and thus arranged in helices. Figures S3 and S4 illustrate the geometric relationship between the NPs and the underlying peptide. The two helices have the same axis and pitch but different helical radii and pitch angles. The same helical pitch means that the two helices have the same helical frequency, based on the relationship $\omega = 2\pi/P$, where P is the helical pitch. Therefore, the NP arrangement can be described using the parametric equations of a helix as follows:

$$x(t) = (R_0 + r)\sin(\omega_0 t + \varphi) \quad (1)$$
$$y(t) = (R_0 + r)\cos(\omega_0 t + \varphi)$$
$$z(t) = t$$

Here, R_0 and r are the superhelical radius of the peptide/SWNT assembly and the radius of NPs, respectively; ω_0 is the superhelical frequency; and φ is the superhelical phase offset. The helical pitch of NPs, P, was computed to be 29.42 nm from the simulated model with the parametric equations.

The interparticle distance in three dimensions was calculated by the equation

$$d = \sqrt{(x_2 - x_1)^2 + (y_2 - y_1)^2 + (z_2 - z_1)^2} \quad (2)$$

where the coordinates (x_1, y_1, z_1) and (x_2, y_2, z_2) are the positions of two particles.

Model Selection for the Structure-Function Correlation Study.

To demonstrate the model prediction accuracy, we measured an electrochemical response generated from a spatially precise arrangement of AuPt NPs and correlated it with the structural feature of the arrangement. Among the two categorized models, the three-helix model is more amenable to the correlation study due to its lower complexity in regulating interparticle distance. For the interparticle distance calculation, the computational models depicted in Figure 2a were used. The geometry of three first-nearest neighboring NPs adjacent to a central NP dictates the interfacial interparticle distances.The distances between NPs at the alanine coil-like, leucine zipper-like, and end-to-end helical interfaces were computed (Figure 2b). All calculated distances are different for individual submodels within the 3 × 2-fold helical array. For the three-fold array, the leucine–leucine interfacial interparticle distance is invariant in all submodels. The other two distances, the intrahelical NP spacing at the alanine–alanine and end-to-end interfaces, aligned along the SWNT axis, are the only variables that determine the interparticle distance, reducing the complexity in interpreting the effect of interparticle distance on the electrochemical response. Thus, we chose the three-helix model to test the structure–function correlation efficiently.

Preparation of AuPt/Peptide/SWNT Superstructures.

The peptide/SWNT suspension was treated with 1 mM of TCEP to reduce the sulfhydryl group of cysteine. The TCEP-treated suspension was purified by centrifugal filtration (Amicon Ultra-4 centrifugal filter with Ultracel-10 membrane) and redispersed in 100 μL of buffer solution (20 mM sodium phosphate and 150 mM NaCl). Next, 10 μL of each precursor solution (100 mM $HAuCl_4$ and 100 mM N_2PtCl_6 in DW) was successively added to the solution and incubated at 4 °C for ~30 min, followed by the slow injection of 40 μL of 100 mM $NaBH_4$, as a reducing agent, into the solution. The reduction reaction was performed at 4 °C to slowly grow nuclei into NPs, directing their assembly into the well-

organized superstructure around the peptide/SWNT template. The reaction times were 10, 24, 48, and 96 h to obtain different sizes of NPs.

Electron Tomography and Three-Dimensional Reconstruction.

The AuPt/peptide/SWNT superstructure samples were placed on the 100 mesh carbon-coated copper grid, and the grid with samples was placed on a double tilting holder; the zero-loss images were viewed using an in-column ω filter equipped Bio-High Voltage Electron Microscope (Bio-HVEM) at 1000 kV (JEM-1000BEF, JEOL, Tokyo, Japan). The region of interest was selected, and the sample was tilted from +50° to –50° with 2° increments. A total of 51 tilt images were recorded by TEM Recorder software (JEOL System Technology Co., Ltd., Tokyo, Japan), and the digitized tilt series images were aligned and tomographically reconstructed using Composer and Visualizer-Kai software (TEMography.com, System in Frontiers Inc., Tokyo, Japan) with no fiducial markers. Subsequently, virtual tomographic slices were extracted from the reconstructed 3-D tomogram, and the boundaries of the region of interest that were visible in each tomographic slice were traced as contours overlaid on the image. The object surface rendering and 3-D volume modeling were performed using the AMIRA software (FEI, Hillsboro, OR).

Electrochemical Measurements of AuPt/Peptide/SWNT Samples.

All electrochemical measurements were carried out in a three-electrode cell at room temperature using a potentiostat (Ivium Compactstat) equipped with a rotating disk electrode system (Metrohm Autolab). Then, 5 μL of AuPt/peptide/SWNT suspension was dropped onto a glassy carbon disk (diameter = 3 mm) and dried naturally, and 5 μL of a 0.05 wt % Nafion (dissolved in ethanol) solution was then dropped. After solvent evaporation in air, a thin layer of the suspension remained on the carbon disk surface to serve as the working electrode. The working electrode was electrochemically cleaned prior to each measurement. A Pt net was used as the counter electrode, and a commercial Hg/HgO/20% KOH electrode (BAS Inc. RE-6A) was used as the reference electrode. All potentials are referred to a reversible hydrogen electrode (RHE).

Cyclic voltammetry (CV) was performed in 0.1 M KOH aqueous solution, deoxygenated by N_2 gas, at a sweep rate of 50 mV s^{-1} (Figure S11). The electrochemically active surface area (ECSA) of Pt was calculated by integrating the area associated with H^+ desorption region after double-layer correction and using a conversion factor of 210 μC cm^{-2} for polycrystalline Pt.[43] The ECSA of Au was calculated in a similar way by measuring the charge collected in the Au reduction region (monolayer of $Au(OH)_2$ or AuO) with a conversion factor of 390 μC cm^{-2} for polycrystalline Au.[44] The polarization curves of oxygen reduction reaction (ORR) were obtained by linear sweep voltammetry in O_2-saturated 0.1 M KOH electrolyte at a sweep rate of 10 mV s^{-1} and a rotation speed of 1600 rpm. The ORR potential was swept from 1.1 to 0.2 V versus RHE.

Supplementary Material

Refer to Web version on PubMed Central for supplementary material.

ACKNOWLEDGMENTS

This research was also supported by Multi-Ministry Collaborative R&D program (Development of Techniques for Identification and Analysis of Gas Molecules to Protect Against Toxic Substances) through the National Research Foundation of Korea (NRF) funded by KNPA, MSIT, MOTIE, ME, NFA (2017M3D9A1073494). This work was also supported by IBS-R015-D1 and the KIST Institutional Program (Project No. 2E27833–18-063).

REFERENCES

(1). Busseron E; Ruff Y; Moulin E; Giuseppone N Supra-molecular Self-assemblies as Functional Nanomaterials. Nanoscale 2013, 5, 7098–7140. [PubMed: 23832165]

(2). King NP; Sheffler W; Sawaya MR; Vollmar BS; Sumida JP; Andre I; Gonen T; Yeates TO; Baker D Computational Design of Self-Assembling Protein Nanomaterials with Atomic Level Accuracy. Science 2012, 336, 1171–1174. [PubMed: 22654060]

(3). Zhang SG Fabrication of Novel Biomaterials through Molecular Self-assembly. Nat. Biotechnol. 2003, 21, 1171–1178. [PubMed: 14520402]

(4). Chen CL; Zhang PJ; Rosi NL A New Peptide-Based Method for the Design and Synthesis of Nanoparticle Superstructures: Construction of Highly Ordered Gold nanoparticle double helices. J. Am. Chem. Soc. 2008, 130, 13555–13557. [PubMed: 18800838]

(5). Chen CL; Rosi NL Preparation of Unique 1-D Nanoparticle Superstructures and Tailoring their Structural Features. J. Am. Chem. Soc. 2010, 132, 6902–6903. [PubMed: 20429558]

(6). Song CY; Wang Y; Rosi NL Peptide-Directed Synthesis and Assembly of Hollow Spherical CoPt Nanoparticle Superstructures. Angew. Chem., Int. Ed. 2013, 52, 3993–3995.

(7). Whaley SR; English DS; Hu EL; Barbara PF; Belcher AM Selection of Peptides with Semiconductor Binding Specificity for Directed Nanocrystal Assembly. Nature 2000, 405, 665–668. [PubMed: 10864319]

(8). Djalali R; Chen YF; Matsui H Au Nanocrystal Growth on Nanotubes Controlled by Conformations and Charges of Sequenced Peptide Templates. J. Am. Chem. Soc. 2003, 125, 5873–5879. [PubMed: 12733928]

(9). Yamashita K; Kirimura H; Okuda M; Nishio K; Sano KI; Shiba K; Hayashi T; Hara M; Mishima Y Selective Nanoscale Positioning of Ferritin and Nanoparticles by Means of Target-Specific Peptides. Small 2006, 2, 1148–1152. [PubMed: 17193580]

(10). Sharma N; Top A; Kiick KL; Pochan DJ One Dimensional Gold Nanoparticle Arrays by Electrostatically Directed Organization Using Polypeptide Self-Assembly. Angew. Chem. Int. Ed. 2009, 48, 7078–7082.

(11). Auyeung E; Morris W; Mondloch JE; Hupp JT; Farha OK; Mirkin CA Controlling Structure and Porosity in Catalytic Nanoparticle Superlattices with DNA J. Am. Chem. Soc. 2015, 137, 1658–1662. [PubMed: 25611764]

(12). Chen W; Bian A; Agarwal A; Liu LQ; Shen HB; Wang LB; Xu CL; Kotov NA Nanoparticle Superstructures Made by Polymerase Chain Reaction: Collective Interactions of Nanoparticles and a New Principle for Chiral Materials. Nano Lett. 2009, 9, 2153–2159. [PubMed: 19320495]

(13). Fan ZY; Govorov AO Plasmonic Circular Dichroism of Chiral Metal Nanoparticle Assemblies. Nano Lett. 2010, 10, 2580–2587. [PubMed: 20536209]

(14). Kuzyk A; Schreiber R; Fan ZY; Pardatscher G; Roller EM; Hogele A; Simmel FC; Govorov AO; Liedl T DNA-Based Self-Assembly of Chiral Plasmonic Nanostructures with Tailored Optical Response. Nature 2012, 483, 311–314. [PubMed: 22422265]

(15). Liu SQ; Tang ZY Nanoparticle Assemblies for Biological and Chemical Sensing. J. Mater. Chem. 2010, 20, 24–35.

(16). Gao Y; Tang ZY Design and Application of Inorganic Nanoparticle Superstructures: Current Status and Future challenges. Small 2011, 7, 2133–2146. [PubMed: 21626691]

(17). Ye XC; Jin LH; Caglayan H; Chen J; Xing GZ; Zheng C; Doan-Nguyen V; Kang YJ; Engheta N; Kagan CR; Murray CB Improved Size-Tunable Synthesis of Monodisperse Gold Nanorods through the Use of Aromatic Additives. ACS Nano 2012, 6, 2804–2817. [PubMed: 22376005]

(18). Lee SW; Chen S; Suntivich J; Sasaki K; Adzic RR; Shao-Horn Y Role of Surface Steps of Pt Nanoparticles on the Electrochemical Activity for Oxygen Reduction. J. Phys. Chem. Lett.2010, 1, 1316–1320.

(19). Ye XC; Collins JE; Kang YJ; Chen J; Chen DTN; Yodh AG; Murray CB Morphologically Controlled Synthesis of Colloidal Upconversion Nanophosphors and their Shape-Directed Self-Aassembly. Proc. Natl. Acad. Sci U. S. A. 2010, 107, 22430–22435. [PubMed: 21148771]

(20). Kao J; Bai P; Lucas JM; Alivisatos AP; Xu T Size-Dependent Assemblies of Nanoparticle Mixtures in Thin Films. J. Am.Chem. Soc. 2013, 135, 1680–1683. [PubMed: 23327718]

(21). Jones MR; Macfarlane RJ; Lee B; Zhang JA; Young KL; Senesi AJ; Mirkin CA DNA-Nanoparticle Superlattices Formed from Anisotropic Building Blocks. Nat. Mater. 2010, 9, 913–917. [PubMed: 20890281]

(22). Cui CH; Gan L; Heggen M; Rudi S; Strasser P Compositional Segregation in Shaped Pt Alloy Nanoparticles and Their Structural Behaviour during Electrocatalysis. Nat. Mater. 2013, 12, 765–771. [PubMed: 23770725]

(23). Chen GX; Zhao Y; Fu G; Duchesne PN; Gu L; Zheng YP; Weng XF; Chen MS; Zhang P; Pao CW; Lee JF; Zheng NF Interfacial Effects in Iron-Nickel Hydroxide-Platinum Nanoparticles Enhance Catalytic Oxidation. Science 2014, 344, 495–499. [PubMed: 24786074]

(24). Urban JJ; Talapin DV; Shevchenko EV; Kagan CR; Murray CB Synergismin Binary Nanocrystal Superlattices leads to Enhanced p-type Conductivity in Self-Assembled PbTe/Ag-2 Te Thin Films. Nat. Mater. 2007, 6, 115–121. [PubMed: 17237786]

(25). Fu XY; Wang Y; Huang LX; Sha YL; Gui LL; Lai LH; Tang YQ Assemblies of Metal Nanoparticles and Self-Assembled Peptide Fibrils - Formation of Double Helical and Single-Chain Arrays of Metal Nanoparticles. Adv. Mater. 2003, 15, 902–906.

(26). Naik RR; Jones SE; Murray CJ; McAuliffe JC; Vaia RA; Stone MO Peptide Templates for Nanoparticle Synthesis Derived from Polymerase Chain Reaction-Driven Phage Display. Adv. Funct. Mater. 2004, 14, 25–30.

(27). Aldaye FA; Sleiman HF Dynamic DNA Templates for Discrete Gold Nanoparticle Assemblies: Control of Geometry, Modularity, Write/Wrase and Structural Switching. J. Am. Chem. Soc. 2007, 129, 4130–4131. [PubMed: 17367141]

(28). Sharma J; Chhabra R; Cheng A; Brownell J; Liu Y; Yan H Control of Self-Assembly of DNA Tubules Through Integration of Gold Nanoparticles. Science 2009, 323, 112–116. [PubMed: 19119229]

(29). Kim J; Lee SW; Carlton C; Shao-Horn Y Pt-Covered Multiwall Carbon Nanotubes for Oxygen Reduction in Fuel Cell Applications. J. Phys. Chem. Lett. 2011, 2, 1332–1336. [PubMed: 26295431]

(30). Slocik JM; Govorov AO; Naik RR Photoactivated Biotemplated Nanoparticles as an Enzyme Mimic. Angew. Chem., Int. Ed. 2008, 47, 5335–5339.

(31). Lee YJ; Yi H; Kim WJ; Kang K; Yun DS; Strano MS; Ceder G; Belcher AM Fabricating Genetically Engineered High-Power Lithium-Ion Batteries Using Multiple Virus Genes. Science 2009, 324, 1051–1055. [PubMed: 19342549]

(32). Shen CQ; Lan X; Lu XX; Meyer TA; Ni WH; Ke YG; Wang Q Site-Specific Surface Functionalization of Gold Nanorods Using DNA Origami Clamps. J. Am. Chem. Soc. 2016, 138, 1764–1767. [PubMed: 26824749]

(33). Zhou BB; Sun ZF; Li D; Zhang T; Deng L; Liu YN Platinum Nanostructures via Self-Assembly of an Amyloid-Like Peptide: a Novel Electrocatalyst for the Oxygen Reduction. Nanoscale 2013, 5, 2669–2673. [PubMed: 23463381]

(34). Ko YS; Kim YT; Kim JH; Kim DH; Kim KH; Yun WS; Kim YD; Lee J; Kim YH Peptide-Based Bimetallic Nanostructures with Tailored Surface Compositions and Their Oxygen Electroreduction Activities. CrystEngComm 2016, 18, 6024–6028.

(35). Grigoryan G; Kim YH; Acharya R; Axelrod K; Jain RM; Willis L; Drndic M; Kikkawa JM; DeGrado WF Computational Design of Virus-Like Protein Assemblies on Carbon Nanotube Surfaces. Science 2011, 332, 1071–1076. [PubMed: 21617073]

(36). Luo J; Njoki PN; Lin Y; Wang LY; Zhong CJ Activity-Composition Correlation of AuPt Alloy Nanoparticle Catalysts in Electrocatalytic Reduction of Oxygen. Electrochem. Commun. 2006, 8, 581–587.

(37). Shao MH; Peles A; Shoemaker K Electrocatalysis on Platinum Nanoparticles: Particle Size Effect on Oxygen Reduction Reaction Activity. Nano Lett. 2011, 11, 3714–3719. [PubMed: 21806027]

(38). Perez-Alonso FJ; McCarthy DN; Nierhoff A; Hernandez-Fernandez P; Strebel C; Stephens IEL; Nielsen JH; Chorkendorff I The Effect of Size on the Oxygen Electroreduction Activity of Mass-Selected Platinum Nanoparticles. Angew. Chem. Int. Ed. 2012, 51, 4641–4643.

(39). Stephens IEL; Bondarenko AS; Gronbjerg U; Rossmeisl J; Chorkendorff I Understanding the Electrocatalysis of Oxygen Reduction on Platinum and Its Alloys. Energy Environ. Sci. 2012, 5, 6744–6762.

(40). Sneed BT; Young AP; Tsung CK Building Up Strain in Colloidal Metal Nanoparticle Catalysts. Nanoscale 2015, 7, 12248–12265. [PubMed: 26147486]

(41). Calle-Vallejo F; Tymoczko J; Colic V; Vu QH; Pohl MD; Morgenstern K; Loffreda D; Sautet P; Schuhmann W; Bandarenka AS Finding Optimal Surface Sites on Heterogeneous Catalysts by Counting Nearest Neighbors. Science 2015, 350, 185–189. [PubMed: 26450207]

(42). Debe MK Electrocatalyst Approaches and Challenges for Automotive Fuel Cells. Nature 2012, 486, 43–51. [PubMed: 22678278]

(43). Sheng WC; Myint M; Chen JGG; Yan YS Correlating the Hydrogen Evolution Reaction Activity in Alkaline Electrolytes with the Hydrogen Binding Energy on Monometallic Surfaces. Energy Environ. Sci. 2013, 6, 1509–1512.

(44). Tremiliosi-Filho G; DalTAntonia LH; Jerkiewicz G Limit to Extent of Formation of the Quasi-Two-Dimensional Oxide State on Au Electrodes. J. Electroanal. Chem. 1997, 422, 149–159.

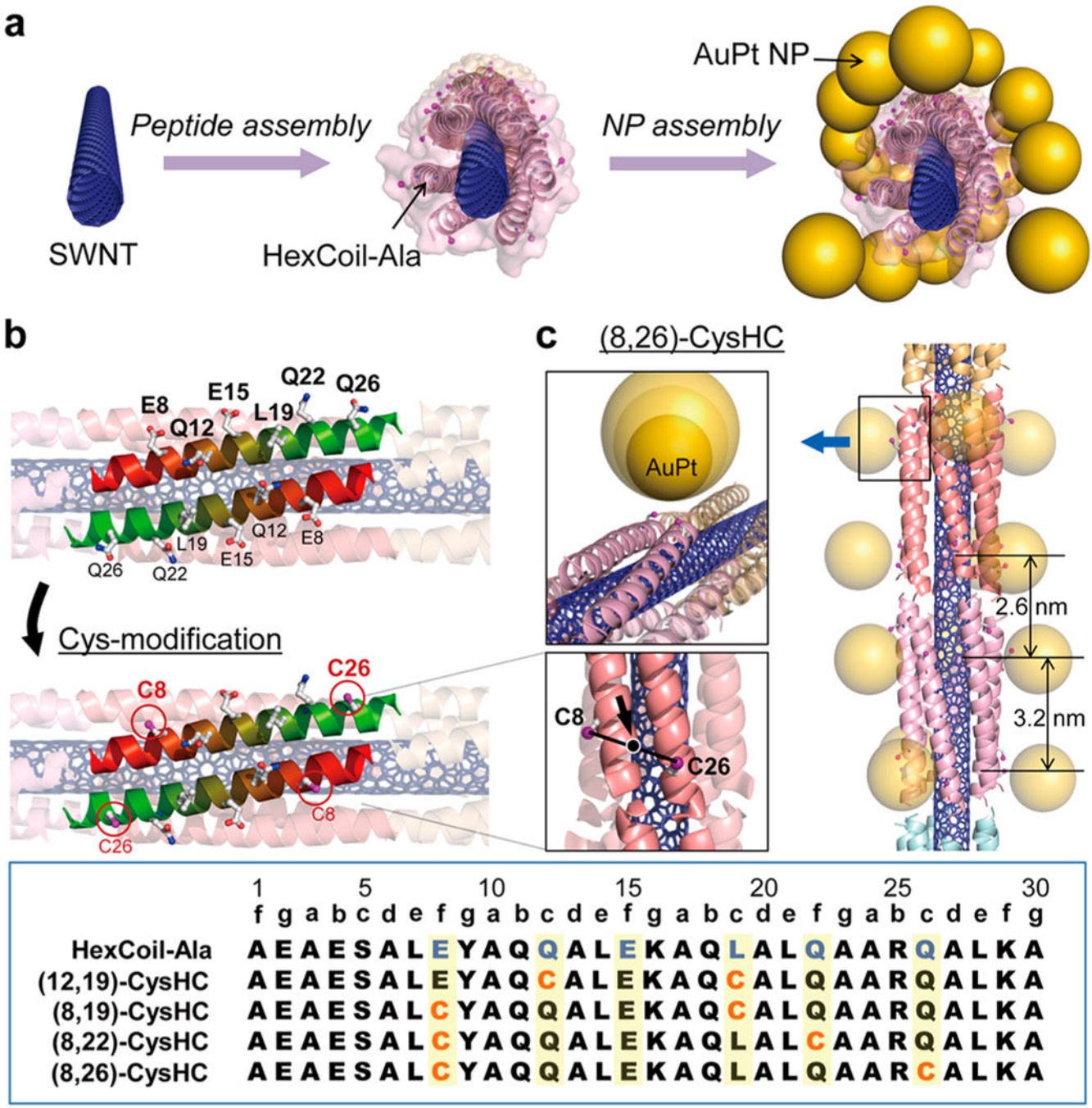

Figure 1.

Peptide-mediated synthesis of NP superstructures on a SWNT. (a) Synthetic scheme. (b) Genetic modification of outward-facing sites in peptide sequences (the red-to-green coloring indicates the N-to-C termini) with Cys residues for specific nucleating NPs. One of the modified peptides, with E8 and Q26 changed to Cys, is shown (bottom box: peptide sequence). (c) Computational model depicting the assembly geometry of (8,26) NPs. The midpoint between two adjacent Cys residues indicates the NP position (inset figures).

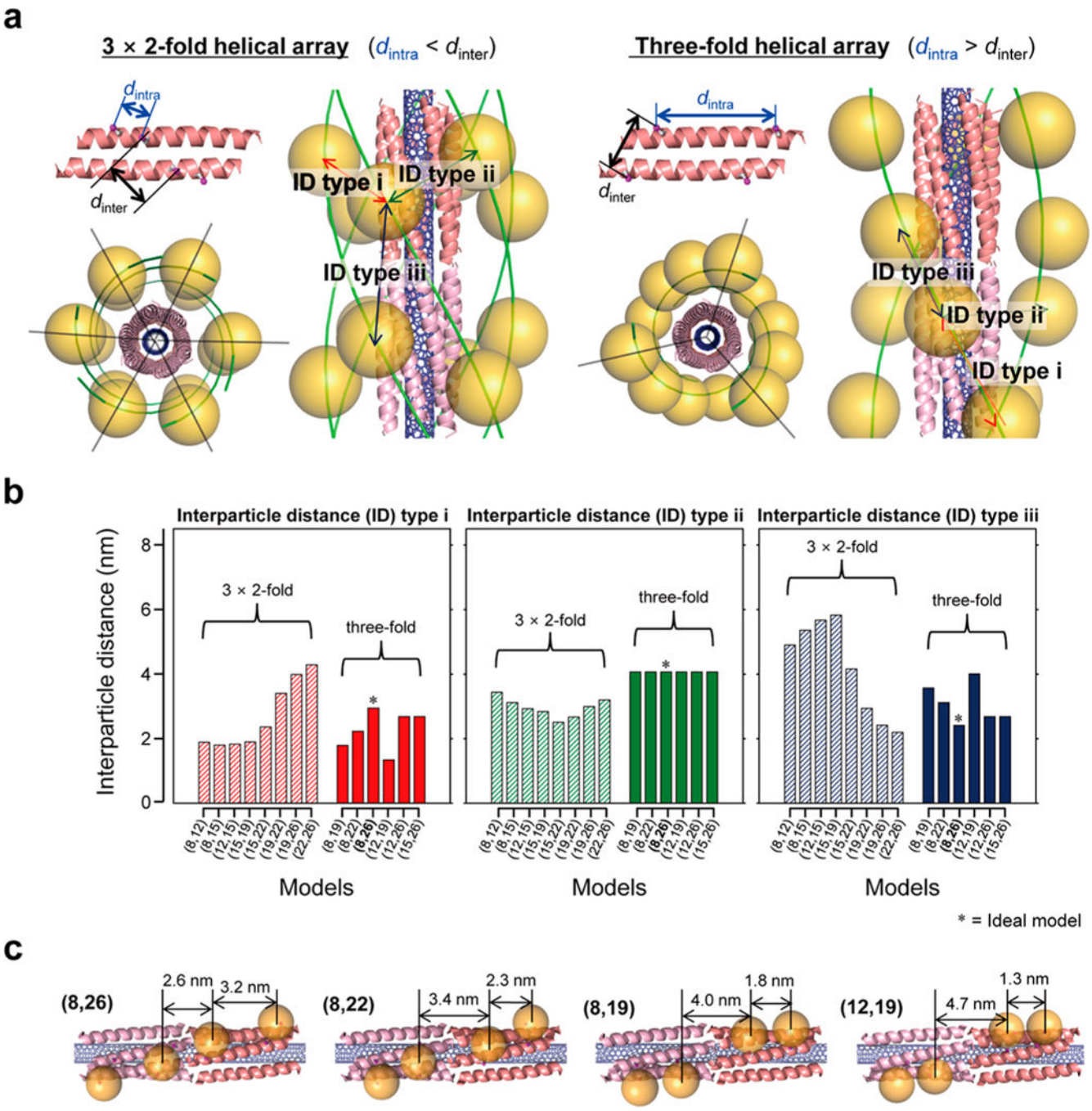

Figure 2.

Two types of helical NP superstructures defining interparticle distances formed by antiparallel six-helix bundles. (a) Antiparallel dimeric unit cells in which two distinct Cys–Cys distances (d_{intra}, on a monomer; d_{inter}, between monomers) are defined to determine the arrangement of NPs in helical geometries, and top-down and side views of computational models of 3 × 2-fold and three-fold helical arrays. (b) Calculated distances between a centrally situated NP and its three first-nearest neighbors (interparticle distance (ID) type i, ID type ii, and ID type iii, indicated by the arrows in part a) for all the submodels. Striped

and solid bars indicate 3 × 2- and three-fold helical array models, respectively. (c) Four different computational models predicting the geometry of an NP assembly aligned on the peptide/SWNT superhelix, highlighting the interparticle distances.

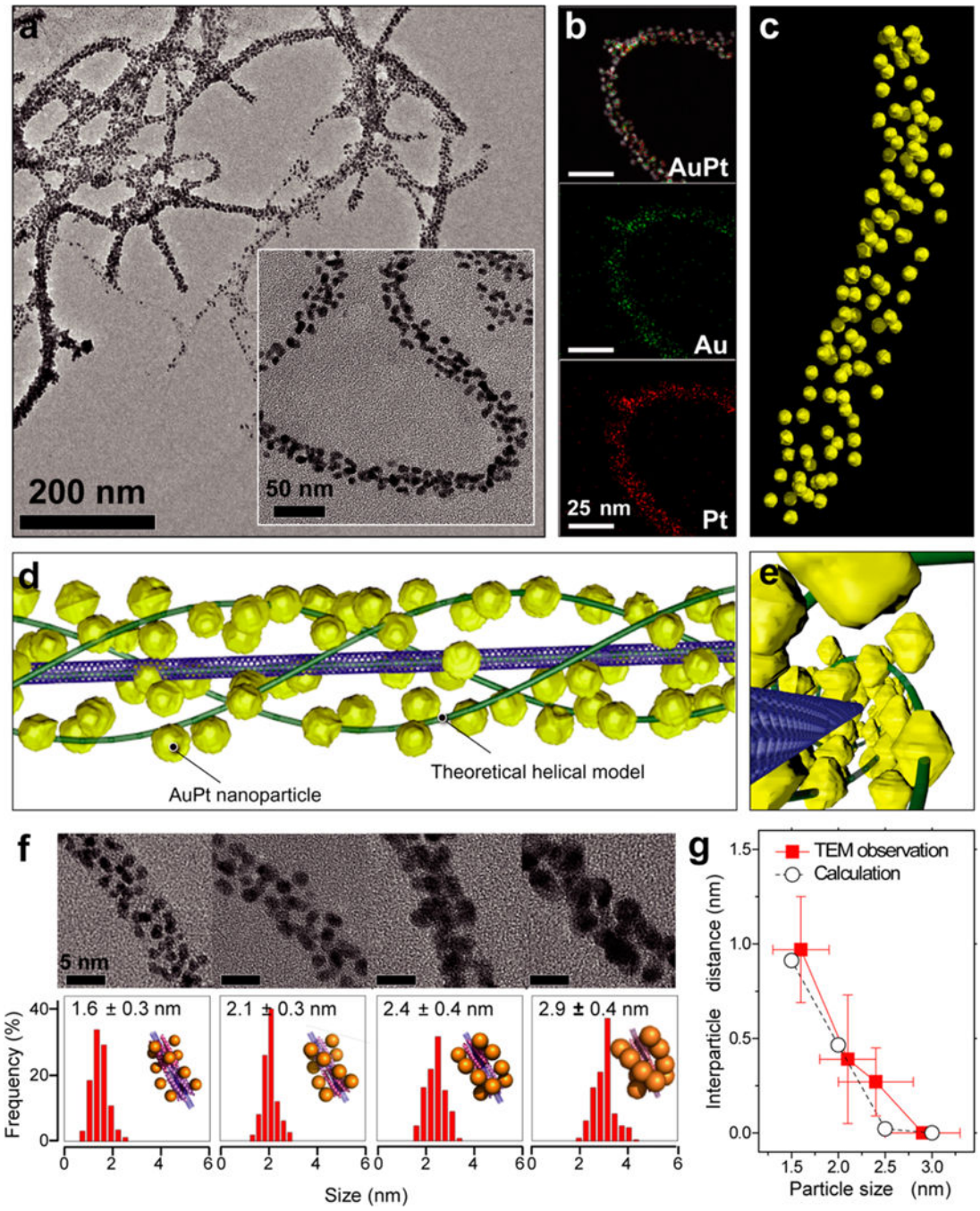

Figure 3.

Characterization of AuPt/HC/SWNT superstructures: (a) TEM and HRTEM images and (b) STEM-EDS elemental mapping images of the (8,26)-modeled sample. (c) 3-D reconstructed model of rendered tomographic volume through electron tomography. (d) Comparison of helical-bundle parametric model based on the theoretical geometries with 3-D reconstruction model. The correlation is shown between the AuPt NPs (yellow dots) and theoretical helical model (green line) both in plane and (e) vertical views. (f) Statistical analysis of the particle size distribution in TEM images of the (8,26)-modeled AuPt/HC/SWNT samples with

average particle sizes of 1.6, 2.1, 2.4, and 2.9 nm (for particle counts >200). (g) Plots of calculated and observed interparticle distances as a function of particle size. The calculated distance data were obtained from simulated models. The observed distances were obtained by subtracting the average particle size from the average center-to-center distance between two particles in TEM images. The center-to-center distances longer than theoretically possible were excluded from the calculation, reducing errors.

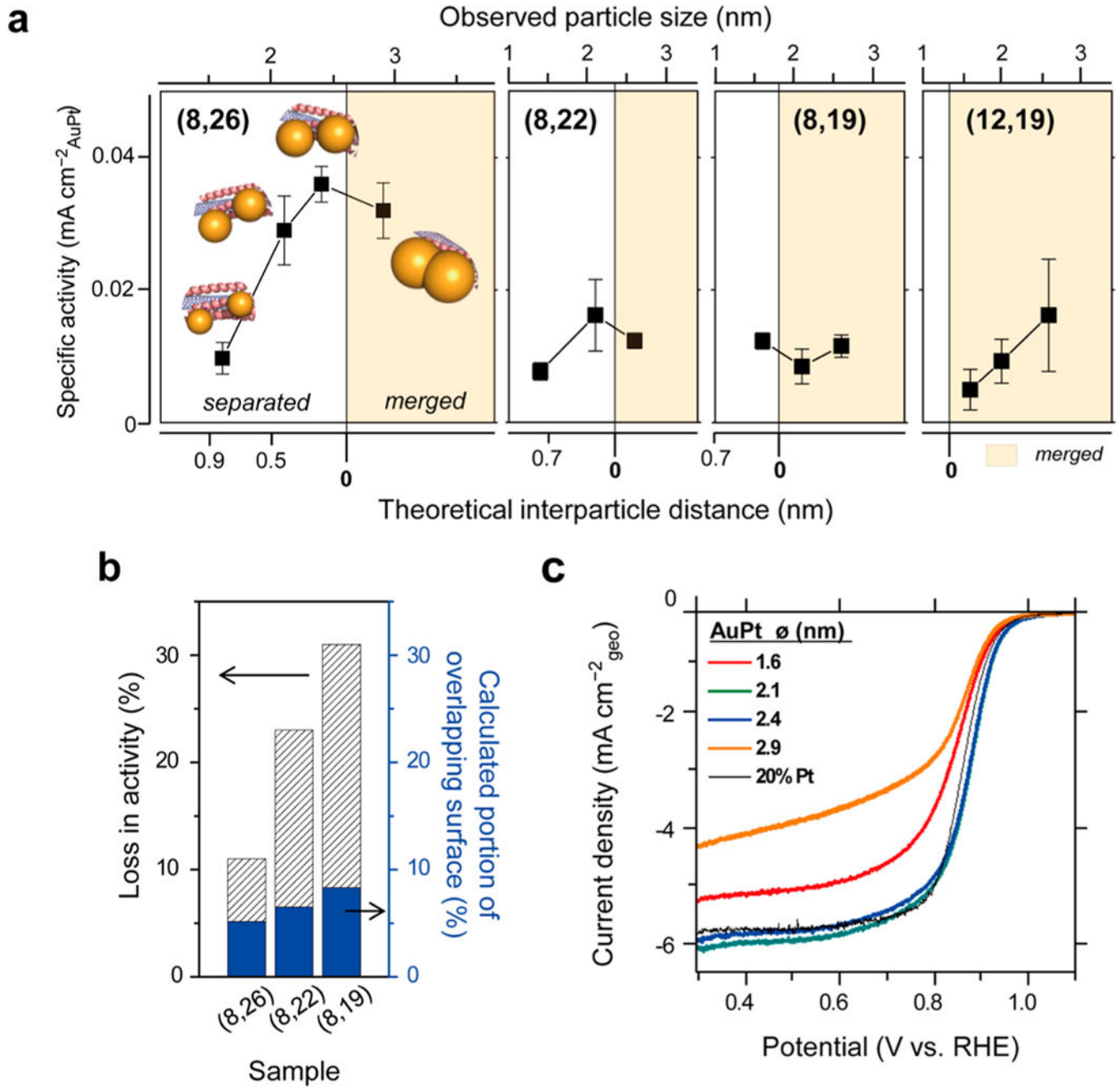

Figure 4.

(a) Specific activities of (8,26), (8,22), (8,19), and (12,19) for these samples at 0.9 V (with respect to a reversible hydrogen electrode, RHE), averaged for four different electrodes. The particle size and interparticle distance were obtained from TEM imaging and model-simulated results, respectively. The areas marked in pale yellow indicate the expected merging of NPs. (b) Loss of specific activities and calculated portion of overlapping surface between AuPt NPs for (8,19), (8,22), and (8,26). The losses were determined using the relationship $[(j_{k,f} - j_{k,m})/j_{k,m}] \times 100$, where $j_{k,m}$ and $j_{k,f}$ are the specific activities of each model before and after particle merging, respectively. The portion of the overlapped surface

area was calculated using the formula for the surface area of a sphere intersected by a plane (see Supporting Information Figure S8). (c) ORR polarization curves of the (8, 26)-catalysts with different particle sizes and a commercial Pt/C catalyst (Premetek, 20% Pt) on a rotating disk electrode in an O_2-saturated 0.1 M KOH solution at a sweep rate of 10 mV s^{-1} and a rotation rate of 1600 rpm.